

1 **Wind extraction potential from ensemble Kalman filter**
2 **assimilation of stratospheric ozone using a global shallow**
3 **water model**

4
5 **D. R. Allen¹, K. W. Hoppel¹ and D. D. Kuhl¹**

6 [1]{Remote Sensing Division, Naval Research Laboratory, Washington, DC, USA}

7 Correspondence to D. R. Allen (douglas.allen@nrl.navy.mil)

8 **Abstract**

9
10 The feasibility of extracting wind information from stratospheric ozone observations is tested
11 using ensemble Kalman filter (EnKF) data assimilation (DA) and a global shallow water model
12 that includes advection of an ozone-like tracer. Simulated observations are created from a truth
13 run (TR) that resembles the Northern Hemisphere winter stratosphere with a polar vortex
14 disturbed by planetary-scale wave forcing. Ozone observations mimic sampling of a polar-
15 orbiting satellite, while geopotential height observations are randomly placed in space and time.
16 EnKF experiments are performed assimilating ozone, height, or both, over a 10 day period. The
17 DA is also implemented using two different pairs of flow variables: zonal and meridional wind
18 (EnKF- uv) and streamfunction and velocity potential (EnKF- $\psi\chi$). Each experiment is tuned for
19 optimal localization length, while the ensemble spread is adaptively inflated using the TR. The
20 experiments are evaluated using the maximum wind extraction potential (WEP). Ozone-only
21 assimilation improves winds (WEP = 46% for EnKF- uv , and 58% for EnKF- $\psi\chi$), but suffers
22 from spurious gravity wave generation. Application of nonlinear normal mode initialization
23 (NMI) greatly reduces the unwanted imbalance and increases the WEP for EnKF- uv (84%) and
24 EnKF- $\psi\chi$ (81%). Assimilation of only height observations also improved the winds (WEP =
25 60% for EnKF- uv , and 69% for EnKF- $\psi\chi$), with much less imbalance compared to the ozone
26 experiment. The assimilation of both height and ozone performed the best, with WEP increasing
27 to ~87% (~90% with NMI) for both EnKF- uv and EnKF- $\psi\chi$, demonstrating that wind extraction
28 from ozone assimilation can be beneficial even in a data-rich environment. Ozone assimilation

1 particularly improves the tropical winds, which are not well constrained by height observations
2 due to lack of geostrophy.

3 **1. Introduction**

4 A key missing component of the global observing system (GOS) is measurement of the three-
5 dimensional global wind (World Meteorological Organization, 2000). Upper air wind
6 observations from radiosondes, pilot reports, and cloud and water vapor feature-tracking leave
7 large gaps, particularly in the tropics, Southern Ocean, and in most of the stratosphere and
8 mesosphere. Spaceborne Doppler Wind Lidar (DWL) has been proposed as the potential
9 “missing link” in the GOS (Baker, 2014). When placed in low earth orbit, DWL can provide
10 daily global wind profiles throughout the troposphere and lower stratosphere (National Research
11 Council, 2007). The Atmospheric Dynamics Mission (ADM-Aeolus) (Stoffelen et al., 2005), will
12 provide a proof-of-concept of this capability. However, the measurements will be limited to a
13 single line-of-sight wind component, altitudes below ~26 km, and simple along-track (as
14 opposed to sweeping or conical) sampling. While future spaceborne DWL missions may provide
15 improved observing capabilities, the technical challenges make this a very difficult and
16 expensive solution to the problem of inadequate wind observations.

17 Another potential source of dynamical information comes from assimilation of trace gas (tracer)
18 observations in a 4-D data assimilation system (DAS) that dynamically couples tracer and wind.
19 The investigation of algorithms to extract wind information from tracers started with 1-D and 2-
20 D simulations by Daley (1995, 1996) and Riishøjgaard (1996). These studies showed that wind
21 information could be extracted from tracer observations when the continuity equation was
22 coupled to the dynamical equations via either a 4D-Var algorithm or an extended Kalman filter
23 (EKF). Extensions to the full 3-D atmosphere were performed in 4D-Var experiments by Peuch
24 et al. (2000), Semane et al. (2009), and Allen et al. (2013). These further supported the potential
25 of tracer assimilation to benefit the winds, but also highlighted limitations due to paucity of
26 observations, insufficient data quality, and inadequate modeling of tracers in the forecast model,
27 as well as phenomenological limitations due to geophysical variability.

28 Assimilation of infrared and microwave humidity channels from geostationary and polar-orbiting
29 satellites has been shown to benefit tropospheric analyses and forecasts in the European Centre

1 for Medium-Range Weather Forecasts (ECMWF) 4D-Var system (Andersson et al., 2007;
2 Peubey and McNally, 2009). Peubey and McNally (2009) isolated the mechanisms whereby
3 geostationary clear-sky radiances can impact the wind analyses in 4D-Var and showed that the
4 dominant factor involves adjustment of the wind field to match observed humidity features (the
5 so-called “tracer advection effect”). However, attempts to assimilate stratospheric ozone using
6 4D-Var algorithms and the resultant dynamical coupling have previously resulted in problems in
7 operational numerical weather prediction (NWP) (Han and McNally, 2010; Dragani and
8 McNally, 2013). These assimilation challenges led Allen et al. (2014) to re-examine the
9 stratospheric tracer-wind problem at a more fundamental level using 4D-Var assimilation studies
10 with a shallow water model (SWM) coupled to the tracer continuity equation. This idealized
11 system allowed Allen et al. (2014) to probe the limits of wind extraction from assimilation of
12 three readily-measured long-lived tracers: ozone (O₃), nitrous oxide (N₂O), and water vapor. It
13 was shown that assimilation of global hourly tracer data was sufficient to analyze the horizontal
14 wind components to a high degree of accuracy ($\sim 0.3 \text{ m s}^{-1}$ random error for O₃ and N₂O).

15 While 4D-Var couples tracers and dynamical variables through the tangent linear model and its
16 adjoint, the initial background error covariance normally does not include tracer-wind
17 correlations (these correlations develop implicitly over the assimilation window). This limitation
18 may be overcome by using an ensemble Kalman filter (EnKF) in which the error covariance
19 between tracer and wind is explicitly calculated by the ensemble statistics. Milewski and Bourqui
20 (2011) assimilated ozone and temperature profiles in an EnKF system using a 3-D model at
21 relatively low resolution (spectral triangular truncation T21). They showed that background error
22 covariances are able to propagate information from the observed variables to wind. In particular,
23 assimilation of either ozone or temperature observations in a polar-orbiting sampling pattern
24 significantly improved the wind analysis. Another approach to enhancing the tracer-wind
25 interaction within 4D-Var is to blend the static covariance with a flow-dependent ensemble
26 covariance. This hybrid 4D-Var method is becoming increasingly popular at operational NWP
27 centers (Buehner et al., 2010; Bonavita et al., 2012; Clayton et al., 2013; Kuhl et al., 2013; Kleist
28 and Ide, 2015). We are developing a hybrid system within the SWM framework to study tracer-
29 wind interaction, which we plan to present in a follow-up paper.

1 In this paper, we take a similar approach to Milewski and Bourqui (2011), except that we use the
2 SWM forecast model (at T42 resolution), and we assimilate ozone and height (in lieu of
3 temperature for the SWM) observations, both separately and together, to examine whether value
4 is added by assimilating ozone observations into a system already constrained by other
5 observations. The SWM has been used in both 4D-Var (Courtier and Talagrand, 1990;
6 Polavarapu et al., 2000; Jung et al., 2014) and EnKF (Kepert, 2009, 2011) experiments, since it
7 provides a sufficiently complex system to simulate the key physical relations of the horizontal
8 flow, including both slow balanced and fast unbalanced modes. As explained by Kepert (2009),
9 the SWM provides a severe test for assimilation, since the weak dissipation will not remove
10 imbalances introduced in the analysis; they will rather accumulate with time.

11 One of the goals of the current study is to probe the limits of ozone-wind extraction in an EnKF
12 system. To accomplish this, it is necessary to quantify (and remove, if possible) spurious
13 imbalance generated from noisy observations and imperfect modeling of background error
14 covariances. A wide range of studies has been performed to examine balance in the context of 4-
15 D data assimilation. For example, Neef et al. (2006, 2009) investigated balance with a low-order
16 Lorenz-type model with the EKF and EnKF. Imbalance within SWM-DAS systems was
17 analyzed in both 4D-Var (Courtier and Talagrand, 1990; Polavarapu et al., 2000) and EnKF
18 (Kepert, 2009, 2011) using digital filter and nonlinear normal mode initialization techniques.
19 Mitchell and Houtekamer (2002) considered the influence of covariance localization on balance
20 with a 3-D dry, global, primitive-equation model. In all of these studies, imbalance was shown to
21 be a serious issue in 4-D DAS. None of these studies was designed to examine balance in the
22 context of the tracer assimilation problem, however. As part of this study we attempt to isolate
23 and to the extent possible remove imbalance in order to minimize the analysis errors and to
24 determine the extent to which the wind can be constrained by ozone observations.

25 The layout of the paper is as follows. Section 2 describes the SWM-DAS, including the forecast
26 model, the EnKF, and the normal mode initialization procedure. Section 3 describes the
27 experimental design and the error diagnostics. Section 4 presents the results and discussion from
28 the three assimilation experiments, and conclusions are provided in Sect. 5.

1 **2. Model description**

2 2.1 Forecast model

3 The forecast model is a spectral SWM based on the vorticity-divergence formulation in Sect. 2a
4 of Ritchie et al. (1988), with the inclusion of fourth-order semi-implicit diffusion applied to the
5 vorticity, divergence, and geopotential. A spectral advection equation is coupled to the SWM,
6 solving for the mixing ratio of a passive tracer as a function of time using the same fourth-order
7 diffusion operator. We call the combined four equation system the shallow water model with
8 tracer (SWM^T). The system is run at triangular truncation T42, with model fields saved on the
9 Gaussian grid (128 longitudes × 64 latitudes, for a grid resolution of ~2.8° at the equator). The
10 discretization uses a leap-frog time integration and a semi-implicit approximation for terms that
11 produce gravity waves (Ritchie, 1988). To restart the model after assimilating data, an Euler
12 forward time stepping method is applied. The global mean geopotential height H is specified to
13 be 10 km, resulting in a gravity wave speed (\sqrt{gH} , where g is the earth's gravitational
14 acceleration) of 313 m s⁻¹. To avoid numerical instability due to gravity waves, a short model
15 time step of 120 s is used for all SWM^T forecasts. The diffusion coefficient is set to 5.0×10^{15} m⁴
16 s⁻¹, which provides an e-folding damping for the highest wavenumber of approximately one day.

17 2.2 Ensemble Kalman filter

18 To assimilate data into the SWM^T system, we use the “perturbed observations” EnKF
19 (Houtekamer and Mitchell, 1998; Evenson, 2003). The system solves for N_{ens} analysis states
20 using the Kalman filter equation for the state vector \mathbf{x} of size N_{state} .

$$\mathbf{x}_i^{\text{a}} = \mathbf{x}_i^{\text{b}} + \mathbf{K}_{\text{ens}} \mathbf{d}_i \quad (1)$$

21 where a and b superscripts indicate analysis and background, and $i = 1 \dots N_{\text{ens}}$ is an index for
22 ensemble member. $\mathbf{d}_i = \mathbf{y}_i - \mathbf{H} \mathbf{x}_i^{\text{b}}$ is the vector of innovations for member i , \mathbf{y}_i is the vector of
23 perturbed observations, and \mathbf{H} is the (linear) observation operator. The ensemble-based Kalman
24 gain matrix is defined as follows

$$\mathbf{K}_{\text{ens}} = \mathbf{P}_{\text{ens}}^{\text{b}} \mathbf{H}^{\text{T}} [\mathbf{H} \mathbf{P}_{\text{ens}}^{\text{b}} \mathbf{H}^{\text{T}} + \mathbf{R}]^{-1} \quad (2)$$

25 with the ensemble background error covariance calculated by

$$\mathbf{P}_{\text{ens}}^{\text{b}} = \frac{1}{N_{\text{ens}} - 1} \sum_{i=1}^{N_{\text{ens}}} (\mathbf{x}_i^{\text{b}} - \overline{\mathbf{x}^{\text{b}}}) (\mathbf{x}_i^{\text{b}} - \overline{\mathbf{x}^{\text{b}}})^T \quad (3)$$

1 Here the overbar indicates the ensemble mean and \mathbf{R} is the observation error covariance matrix.
 2 The background state is calculated using the non-linear SWM^T forecast model M , subject to
 3 initial conditions

$$\mathbf{x}_i^{\text{b}}(t_n) = M[\mathbf{x}_i^{\text{b}}(t_{n-1})] \quad (4)$$

4 where n is an index for model time (t_n). Note that the SWM^T time step (120 s) is less than the
 5 analysis time step (20 min), such that there are 10 forecast model time steps between analyses.
 6 At each analysis time, which corresponds to the end of the 20-minute background forecast, all
 7 the observations at that time are assimilated simultaneously as a single batch.

8
 9 The EnKF analysis equation can be solved using different combinations of state variables. In this
 10 study, we compare results using zonal wind, meridional wind, height, and ozone $\mathbf{x} = [u, v, z, q]$
 11 (the EnKF- uv system) and streamfunction, velocity potential, height, and ozone $\mathbf{x} = [\psi, \chi, z, q]$
 12 (the EnKF- $\psi\chi$ system). The latter combination was shown by Keperter (2009) to result in better
 13 balance of increments in a SWM-EnKF system with Schur product localization (discussed
 14 further below). We will test this for the SWM^T system with ozone and height observations.

15
 16 To avoid filter divergence, we apply a state space covariance inflation factor (Anderson, 2007) to
 17 the background ensemble before assimilating observations. The background ensemble
 18 perturbations ($\mathbf{x}_i^{\text{b}} - \overline{\mathbf{x}^{\text{b}}}$) are multiplied by a scalar factor ξ to produce the inflated background
 19 ensemble

$$\mathbf{x}_i^{\text{b,inf}} = \xi (\mathbf{x}_i^{\text{b}} - \overline{\mathbf{x}^{\text{b}}}) + \overline{\mathbf{x}^{\text{b}}} \quad (5)$$

20 which alters the background error covariance (Eq. 3), but leaves the background ensemble mean,
 21 $\overline{\mathbf{x}^{\text{b}}}$, unchanged. The inflation factor is designed to alter the global average SPREAD to match
 22 the global Root Mean Square Error (RMSE) of either the vector wind (for EnKF- uv) or the
 23 streamfunction (for EnKF- $\psi\chi$). The RMSE and SPREAD for vector wind are defined as

$$V_{\text{RMSE}} = \sqrt{\frac{1}{N_{\text{state}}} \sum_{j=1}^{N_{\text{state}}} [\bar{u}_j^{\text{b}} - u_j^{\text{TR}}]^2 + [\bar{v}_j^{\text{b}} - v_j^{\text{TR}}]^2} \quad (6)$$

$$V_{\text{SPREAD}} = \sqrt{\frac{1}{(N_{\text{ens}} - 1)N_{\text{state}}} \sum_{i=1}^{N_{\text{ens}}} \sum_{j=1}^{N_{\text{state}}} [u_{i,j}^{\text{b}} - \bar{u}_j]^2 + [v_{i,j}^{\text{b}} - \bar{v}_j]^2} \quad (7)$$

2 where V represents the magnitude of the vector wind (V) and TR indicates the truth run
 3 (described in Sect. 3.1). For streamfunction (ψ) the RMSE and SPREAD are defined as

$$\psi_{\text{RMSE}} = \sqrt{\frac{1}{N_{\text{state}}} \sum_{j=1}^{N_{\text{state}}} [\bar{\psi}_j^{\text{b}} - \psi_j^{\text{TR}}]^2} \quad (8)$$

$$\psi_{\text{SPREAD}} = \sqrt{\frac{1}{(N_{\text{ens}} - 1)N_{\text{state}}} \sum_{i=1}^{N_{\text{ens}}} \sum_{j=1}^{N_{\text{state}}} [\psi_{i,j}^{\text{b}} - \bar{\psi}_j]^2} \quad (9)$$

5 The inflation factor is defined as either $\xi_V = V_{\text{RMSE}} / V_{\text{SPREAD}}$ or $\xi_\psi = \psi_{\text{RMSE}} / \psi_{\text{SPREAD}}$. While the
 6 inflation factor is calculated using only the wind or streamfunction, it is applied to the entire state
 7 vector for each ensemble member using Eq. (5). The calculations of RMSE and SPREAD are not
 8 area-weighted, and therefore may be somewhat biased to match the higher latitudes, since the
 9 Gaussian grid is used. This tuning takes a similar approach to the 4D-Var simulations of Allen et
 10 al. (2014) in which the background error variances were modified to match the global RMSE of
 11 the tracer and wind components. This adaptive tuning provides a flexible way to examine how
 12 the system behaves over a wide range of parameters, without needing to separately tune the
 13 inflation factor for each case. It is of course not practical in an operational setting, since the true
 14 state is unknown, but for this idealized study it works well to prevent filter divergence.

15

16 To avoid spurious long-range correlations, localization is applied to the background error
 17 covariance. We apply the elementwise (Schur product) approach (e.g., Houtekamer and Mitchell,
 18 2001) using Eq. (4.10) of Gaspari and Cohn (1999). The localization matrix \mathbf{S} is applied directly
 19 to the background error covariance so the gain matrix becomes

$$\mathbf{K}_{\text{ens}} = \mathbf{S} \circ \mathbf{P}_{\text{ens}}^{\text{b}} \mathbf{H}^{\text{T}} [\mathbf{H} \mathbf{S} \circ \mathbf{P}_{\text{ens}}^{\text{b}} \mathbf{H}^{\text{T}} + \mathbf{R}]^{-1} \quad (10)$$

1 To illustrate the ozone-wind interaction in the SWM^T-EnKF system, Fig. 1 shows the ensemble
2 mean analysis increments $\mathbf{K}_{\text{ens}} \bar{\mathbf{d}}$ for assimilation of a single ozone observation at 120°E
3 longitude, 40°N latitude for the EnKF-*uv* and EnKF- $\psi\chi$ systems. For the EnKF- $\psi\chi$, we convert
4 the increments to wind increments after the analysis step. Specification of the initial 100-member
5 ensemble for this system will be discussed in Sect. 3. The positive ensemble mean ozone
6 innovation ($\bar{\mathbf{d}} = 0.21$ parts per million by volume, ppmv) results in a positive ozone increment in
7 the vicinity of the observation with maximum of 0.11 ppmv. Since the height correlates
8 positively with ozone, a positive height increment also occurs (maximum of 84 m). Note that the
9 ozone and height increments are similar for both systems, since these variables are unchanged;
10 slight differences are due to differences in tuning of the background error covariances. The wind
11 increments are very different, however. While both show anticyclonic circulation around the
12 positive height increment, the winds are much stronger in the EnKF- $\psi\chi$. As explained by Kepert
13 (2009, 2011) the weakening of the winds in the EnKF-*uv* is due the effects of localization, which
14 acts to decrease the local balance. As shown below, this adversely affects the system by
15 generating spurious gravity waves.

16 2.3 Normal mode initialization

17 In general, analysis increments may project onto both slow balanced modes and fast unbalanced
18 modes. Unless there is sufficient information in the background error covariance to distribute
19 increments in a balanced way, the unbalanced modes will enter the system, and it may be
20 difficult to remove these modes with limited observations (Neef et al., 2006, 2009). To quantify
21 the imbalance in the SWM-EnKF, we use a nonlinear normal mode initialization (NMI)
22 procedure (Machenhauer, 1977), which has been used in NWP to reduce the impact of inertia
23 gravity waves caused by imbalance in the analysis increments (e.g., Kleist et al., 2009). While
24 digital filter initialization (e.g., Fillion et al., 1995) is more commonly used in NWP today, NMI
25 allows discrimination between the gravity wave and rotational wave modes, which is very useful
26 in the SWM context. Kepert (2009) used NMI to analyze imbalance caused by localization in the
27 SWM-EnKF framework, and showed that while gravity waves can be reduced by judicious
28 choice of balance constraints, some initialization may still be necessary in the EnKF (see also the
29 discussion in Lorenc, 2003).

30

1 For example, the single-observation increments in Fig. 1 result in unbalanced motions in both
2 versions of the SWM^T system. Figure 2 shows the divergence anomalies due to the single-
3 observation increments. These anomalies propagate radially outward from the observation
4 location, as seen in these maps at 2 h intervals. Maps at later times (not shown) indicate that
5 these oscillations propagate around the globe in ~1.5 days, consistent with waves traveling at the
6 gravity wave phase speed of this system. The EnKF- $\psi\chi$ increments result in smaller divergence
7 fields than the EnKF- uv ; the maximum divergence anomaly at 1200 s for the EnKF- $\psi\chi$ is ~13%
8 of that caused by the EnKF- uv , consistent with less imbalance. However, initialization may still
9 be necessary in both systems to remove this spurious gravity “noise.”

10

11 To “initialize” the system (i.e., apply NMI to the analysis state vector), we first need the normal
12 modes (NM) of the SWM system. These were calculated using the formulation outlined in
13 Hogan et al. (1992). The resulting NM frequencies are shown in Fig. 3 as a function of zonal
14 wavenumber and mode type. Negative (positive) wavenumbers indicate westward (eastward)
15 propagating modes. These modes are separated into westward and eastward gravity wave (GW)
16 and westward rotational wave (RW) modes. To balance the GW modes, we apply the
17 Machenhauer (1977) condition, which reduces the time tendencies of the complex amplitudes of
18 the modes. We apply five iterations to solve the nonlinear balance equation using a single 120 s
19 time step for the calculation of the tendencies. We choose a linear cutoff frequency of 1.0 day⁻¹,
20 which attempts to balance all traveling modes except for one eastward wave 1 GW mode (see
21 Fig. 3a).

22

23 In this study, we apply NMI to the ensemble mean analyzed fields only as a post-processing
24 diagnostic to quantify the degree of imbalance. The goal is to tune the EnKF system to minimize
25 unwanted imbalance, without having to rely on applying NMI within the DAS. One reason to
26 avoid initialization in the EnKF cycling is that it fails to distinguish real and spurious gravity
27 waves, and can therefore potentially move the system away from the truth. Another reason is that
28 running NMI in the EnKF would involve initializing each ensemble member separately, since
29 different modes may be excited in each member due to the perturbed observations, which adds
30 significantly to the computational expense. In principle, if the unbalanced modes do not interact
31 much with the balanced components of the flow, then it should not matter whether the balancing

1 is done before or after the assimilation. Williamson and Temperton (1981), using a multilevel
2 global grid-point model, showed that forecasts made with initialized data produced virtually
3 identical results to forecasts with uninitialized data followed by initialization. This suggests that
4 the high-frequency GW do not interact much with the low-frequency RW, but rather can be
5 largely considered “noise” in the system that can, in principle, be filtered out. To test whether
6 this is true for the system run here, we compared results using NMI cycling and NMI post-
7 processing for the optimal runs of the three experiments examined in Sect. 4. Differences in wind
8 extraction potential (defined in Sect. 3) were $\sim 1\%$ or less for all runs, except for height only
9 assimilation with the EnKF- uv system, which showed an improvement of 5% for NMI cycling
10 over NMI post-processing. Assimilation of height observations is likely more sensitive to GW
11 noise, which impacts the height directly, while the tracer is only indirectly impacted via the
12 divergent component of the wind, which is small compared to the rotational wind.

13
14 To illustrate the influence of NMI post-processing, Fig. 4 shows the true divergence along with
15 the analyzed divergence with and without NMI for a sample field two days into an ozone
16 assimilation run. Whereas the true divergence is rather smooth, the uninitialized divergence
17 shows considerable noise. After applying NMI, the analyzed divergence looks much more like
18 the truth, indicating that the noise was due largely to spurious unbalanced modes. We note that
19 this rather large improvement from application of NMI is partly illustrating sensitivities in the
20 SWM. Whereas in a full NWP system, physical and radiative processes may dampen the gravity
21 waves, in the SWM with weak diffusion, the waves can remain in the system for a long time,
22 unless assimilated data are at sufficient sampling frequency and precision to resolve the waves.

23 **3. Experimental design**

24 **3.1 Truth run**

25 The truth run (TR) is designed to simulate Northern Hemisphere (NH) winter conditions in the
26 middle stratosphere (the same TR was used in the 4D-Var tracer assimilation study by Allen et
27 al., 2014). The initial conditions for the SWM^T include zero meridional wind and a zonally-
28 symmetric zonal wind that varies with latitude (φ) as $u(\varphi) = u_{\max} \sin(2\varphi)$ in the NH and is zero
29 in the Southern Hemisphere (SH), with $u_{\max} = 60 \text{ m s}^{-1}$. The geopotential height is specified

1 using the gradient wind balance with a global mean height of 10 km. The initial ozone is
2 calculated using Aura Microwave Limb Sounder (MLS) ozone data (Waters et al., 1999; Livesey
3 et al., 2011). The data are selected for a period with weak planetary wave activity (1-15 March
4 2011) and are interpolated to the 850 K isentropic level (approximately 32 km altitude or 10
5 hPa), representative of middle stratosphere conditions. The zonal mean and time mean mixing
6 ratio as a function of latitude was calculated for this period and interpolated to the Gaussian grid.
7 The ozone is treated as passive (i.e., no chemical source/sink) and there is no radiative
8 interaction between ozone and dynamics. Note that in the TR there are no “restarts,” since it is a
9 continuous free-running SWM^T forecast. Therefore, an assimilation cycling run, which restarts
10 with a forward Euler step after each 20-minute analysis cycle, would produce a slightly different
11 result from the free-running forecast (which uses leap-frog time integration for all steps after the
12 initial Euler step), even if no data were assimilated. We could, in principle, stop and restart the
13 TR with a forward Euler step at the regular analysis time intervals, as was done in Kepert (2009);
14 however, test runs performed with and without restarts in the TR resulted in negligible
15 differences.

16
17 To create a realistic scenario of the NH winter stratosphere, the TR is forced by the bottom
18 topography being raised and lowered to simulate planetary-scale waves (as in Norton, 1994). A
19 mountain of height 1250 m is created with a 20 day cycle (4 days ramping up, 12 days constant,
20 and 4 days ramping down). The mountain is a zonal wave 1 feature that peaks at 45°N. The
21 topography is turned off after 20 days. Since the assimilation period corresponds to days 20-30
22 of this TR, there is no surface topography during the assimilation. NH maps of the ozone and
23 height fields for the TR are provided in Fig. 5a-f. On day 20, a strong anticyclone (indicated by
24 “H”) is present near 180° longitude, resembling an “Aleutian High,” with elevated ozone values.
25 The polar vortex (indicated by “L”), identified by low ozone, is displaced off the pole into a
26 comma shape. Over the next 10 days, the “Aleutian High” diminishes in strength and the vortex
27 moves over the pole. Strong ozone advection occurs throughout this period. For example, a long
28 tongue of lower ozone mixing ratio forms around a secondary anticyclone centered near 60°E
29 longitude on day 28. This dynamical scenario produced by topographic wave forcing in the
30 SMW^T provides a realistic representation of the final stages of a stratospheric minor warming
31 (Limpasuvan et al., 2004). In the SH (Fig. 5g-l), a strong anticyclone is centered just off the pole

1 on day 20. This anticyclone (“H”) propagates westward around the pole, making one cycle over
2 this 10 d period. A weaker cyclone (“L”) also propagates westward around the pole opposite to
3 the anticyclone. The ozone is advected along with these features, with relatively high (low)
4 ozone in the anticyclone (cyclone). The westward flow in the SH is consistent with the easterly
5 summer flow in the middle stratosphere (Andrews et al., 1987). Additional maps of potential
6 vorticity and ozone for this TR are provided in Fig. 2 of Allen et al. (2014).

7 3.2 Observations

8 Observations are simulated by sampling the TR ozone and height fields using a bi-linear
9 interpolation in latitude and longitude. Gaussian random error is then added with a specified
10 standard deviation (SD). The error SD for ozone was set to 0.08 ppmv, which is 1% of the initial
11 global mean, while the height error SD was set to 50 m. The height error can be approximately
12 related to stratospheric temperature error by using a climatological estimate of the equator-to-
13 pole gradient of temperature with respect to geopotential height in the NH winter middle
14 stratosphere of $\sim 5 \text{ K km}^{-1}$. Using this conversion factor, 50 m error corresponds to $\sim 0.25 \text{ K}$. Both
15 the ozone and height errors are smaller than those of any current operational instrument. The
16 goal here is not to evaluate an actual observing system, but to demonstrate ozone-wind extraction
17 in an idealized system. The observation errors are assumed to be uncorrelated, so the observation
18 error covariance \mathbf{R} is diagonal with elements given by the square of the error SDs.

19
20 Two sampling methods are performed (see Fig. 6). For ozone, the observation locations are taken
21 from real ozone observations from the Aura MLS polar-orbiting satellite (sampling frequency of
22 ~ 3450 observations per day). For height, pseudo-random sampling in space and time is
23 performed to approximate the global coverage provided by microwave and infrared radiance
24 sensors. For each successive height observation, the sampling occurs at one of 3840
25 latitude/longitude points on an icosahedral equal-area grid. This allows the observations to not be
26 too clumped together and provides a way to scale upward to a global equal area grid sampling, as
27 was used in Allen et al. (2013). We choose the average data frequency for the height
28 observations to be the same as the MLS sampling frequency (~ 3450 per day). In time, the height
29 observations occur randomly over 10 days. For both observation types, the observation time is

1 assigned to the nearest 20 min interval (0, 20, or 40 min). Since the analysis is performed
2 sequentially every 20 minutes, time-interpolation is not necessary for observations.

3 3.3 Assimilation experiments

4
5 We use 100 ensemble members for all experiments in this paper. The initial ensemble
6 perturbations are generated by sampling the TR fields at 6 h intervals (starting day 21, 0 h) and
7 then removing the ensemble mean. The assimilation experiments begin 20 days into the TR (day
8 20, 0 h), with the initial ensemble defined as the ensemble perturbations added to the TR field
9 that is offset 6 h from the initial time (i.e., day 20, 6 h), which serves as the initial ensemble
10 mean and defines the initial analysis. This initial 6 h offset, or mismatch, between the TR and the
11 initial background fields is the source of the initial background error. In Sect. 4 we present
12 results from three different experiments: (1) ozone only, (2) height only, and (3) ozone and
13 height. For each experiment, assimilation runs were done for both EnKF- uv and EnKF- $\psi\chi$ using
14 localization lengths from 1000 to 8000 km, in 500 km increments (note that ozone only
15 experiments failed to converge at the maximum localization length of 8000 km). Tuning the
16 length separately for each experiment and EnKF is necessary, since the DA responds differently
17 depending on the field(s) observed and the analysis variables used. For each experiment we use
18 the same localization length for all state variables. Further optimization may occur by applying
19 different localization functions to different variables, but this is beyond the scope of this first
20 study on tracer-wind interaction using the EnKF. Since inflation is automatically adjusted in a
21 self-consistent manner with the TR, it does not require tuning. Post-processing with NMI was
22 also performed for each run. We note here that the same forecast model is used for the TR and
23 for the assimilation experiments (i.e., “identical twin” experiments), making results overly
24 optimistic.

25 3.4 Error metrics

26 To diagnose the results, several error metrics are examined, including the global RMSE (area-
27 weighted) of the u , v , z , and q , along with the Wind Extraction Potential (WEP). Allen et al.
28 (2014) defined WEP as a normalized diagnostic of the impact of tracer assimilation on the
29 dynamics. The WEP is determined by first calculating the analyzed RMSE of the vector wind as
30 a function of latitude (φ) and time (t):

$$V_{\text{RMSE}}(\varphi, t) = \sqrt{[u_{\text{RMSE}}(\varphi, t)]^2 + [v_{\text{RMSE}}(\varphi, t)]^2}, \quad (11)$$

1 where

$$u_{\text{RMSE}}(\varphi, t) = \sqrt{\sum_{\lambda} [u(\lambda, \varphi, t) - u^{\text{TR}}(\lambda, \varphi, t)]^2 / \text{NLON}} \quad (12)$$

3 is RMSE of the zonal wind calculated around a latitude circle containing NLON longitude (λ)
 4 grid points and TR refers to the truth run (the RMSE of the meridional wind, v_{RMSE} , is calculated
 5 similarly). The latitude dependence is shown explicitly here, since we will examine errors as a
 6 function of latitude in Sect. 4. The percentage difference in vector wind error relative to the
 7 initial error is then calculated,

$$V_{\text{DIFF}}(\varphi, t) = \left[\frac{V_{\text{RMSE}}(\varphi, 0) - V_{\text{RMSE}}(\varphi, t)}{V_{\text{RMSE}}(\varphi, 0)} \right] \times 100\%, \quad (13)$$

8 and WEP is defined as the area-weighted global average of this quantity, calculated using

$$\text{WEP}(t) = \sum_{\varphi} V_{\text{DIFF}}(\varphi, t) \cos \varphi / \sum_{\varphi} \cos \varphi, \quad (14)$$

9 where the summation is over all latitudes.

10

11 A WEP value of 100% indicates the analysis equals the truth (i.e., $V_{\text{RMSE}}(\varphi, t) = 0$). Although
 12 WEP is relative to the initial error, and therefore will vary from one experiment design to
 13 another, it provides a useful normalized number for quantitative comparison between runs using
 14 the same initial error. In this paper, all experiments start with the same initial vector wind error
 15 with a global mean value, $\tilde{V}_{\text{RMSE}}(0) = 4.55 \text{ m s}^{-1}$, so WEP can be compared directly among all
 16 runs (tilde refers to the global area-weighted mean). As a rule of thumb, an approximate
 17 conversion from WEP to wind component error can be derived by assuming RMS wind errors do
 18 not vary with latitude and assuming zonal and meridional wind errors are equal. This results in
 19 the following approximation

$$\tilde{u}_{\text{RMSE}}(t) = \tilde{u}_{\text{RMSE}}(0) \times [1 - \text{WEP}(t)/100]. \quad (15)$$

1 The initial global mean zonal wind RMSE, $\tilde{u}_{\text{RMSE}}(0)$, is $\sim 3.3 \text{ m s}^{-1}$, so WEP values of 50, 60, 70,
 2 80, and 90 correspond to approximate wind component errors of 1.65, 1.30, 1.00, 0.66, and 0.33
 3 m s^{-1} , respectively.

4
 5 Experiment errors are generally presented as the “final” error of the 10 day simulations. To
 6 reduce random noise, the final errors are calculated as the average values over the last 24 h of
 7 each simulation. To estimate the statistical uncertainty in the final errors, Experiment 3 was
 8 repeated ten times with different random observation perturbations, with a localization of 3500
 9 km. The SD of the final values was $\sim 0.5\%$ for WEP, $\sim 0.02 \text{ m s}^{-1}$ for the wind components, ~ 0.4
 10 m for height, and $\sim 0.002 \text{ ppmv}$ for ozone. The results in Table 1 are presented with the number
 11 of significant digits that reflect the uncertainties determined from this test.

12
 13 The final diagnostic is designed to measure the amount of gravity wave “noise” in the system,
 14 also called “imbalance.” Imbalance is defined here using the uninitialized height z_{uninit} and
 15 initialized height z_{init} (i.e., after NMI has been applied). As with WEP, we first calculate the
 16 RMS difference between these two fields as a function of latitude

17

$$z_{\text{RMS}}(\varphi, t) = \sqrt{\sum_{\lambda} [z_{\text{uninit}}(\lambda, \varphi, t) - z_{\text{init}}(\lambda, \varphi, t)]^2 / \text{NLON}}, \quad (16)$$

18 and then we calculate the area-weighted global mean,

$$\text{Imbalance}(t) = \sum_{\varphi} z_{\text{RMS}}(\varphi, t) \cos \varphi / \sum_{\varphi} \cos \varphi. \quad (17)$$

19 We note here that the TR used in this paper contains negligible gravity wave amplitudes at
 20 frequencies higher than 1.0 day^{-1} . The imbalance calculated by applying NMI to the TR is less
 21 than 1 m. So any imbalance greater than $\sim 1 \text{ m}$ is due to spurious GW generation.

1 4. Results and discussion

2 4.1 Experiment 1: ozone only

3 In this section, we examine the performance of the SWM^{T} -EnKF system when ozone data are
4 assimilated alone. Figure 7 shows time series of error diagnostics for the two “optimal” runs
5 from Experiment 1 (tuning of the covariance localization to determine the optimal run is
6 described later in this section). Results are presented both for uninitialized (solid lines) and
7 initialized (NMI, dotted lines) output. The uninitialized WEP steadily increases before leveling
8 off at final values of $\sim 46\%$ for EnKF- uv and $\sim 58\%$ for EnKF- $\psi\chi$, with corresponding wind
9 component errors of $\sim 1.6 \text{ m s}^{-1}$ and $\sim 1.3 \text{ m s}^{-1}$. Most of the improvement occurs during the first
10 five days. After applying NMI to these runs, the initialized WEP increases significantly for both
11 systems, indicating that imbalance is limiting the wind improvement and error reduction.

12
13 The uninitialized height error for EnKF- uv levels out at $\sim 61 \text{ m}$, while for EnKF- $\psi\chi$, the
14 uninitialized height error reaches $\sim 43 \text{ m}$. Much of the height error can be attributed to GW
15 generated in the system. Figure 7e shows that the imbalance starts near zero, but increases as
16 GW are introduced into the system. For EnKF- uv , the imbalance rises rapidly over the first two
17 days until it nearly matches the uninitialized height error. After this time, the further growth of
18 GW is likely restrained by the weak dissipation in the SWM^{T} system. For EnKF- $\psi\chi$, the
19 imbalance grows more slowly, but is still close to the uninitialized height error at the end.
20 Because the uninitialized height error and imbalance are still increasing at the end of 10 days,
21 this suggests that the GW have not saturated for EnKF- $\psi\chi$. Application of NMI results in
22 dramatically reduced height errors for both systems. There is an ~ 1 day oscillation in the
23 initialized height errors, which is largely due to the one traveling eastward GW mode that is not
24 initialized, which is present in the TR. The decreasing amplitude of the oscillation with time
25 suggests that this mode is being resolved by the system through the ozone-wind extraction.

26
27 The ozone errors (Fig. 7f) show a sharp decrease over the first day, followed by a gradual
28 decline. Although the errors in the dynamical variables have leveled out by day 10, the ozone
29 errors appear to still be declining. Both runs show final ozone errors less than the observation
30 error of 0.08 ppmv . As a global consistency check of the EnKF solution, we also calculated

$$\overline{\chi^2} = \bar{\mathbf{d}}^T [\mathbf{H}\mathbf{P}_{\text{ens}}^b \mathbf{H}^T + \mathbf{R}]^{-1} \bar{\mathbf{d}} \times (\text{NOBS})^{-1}, \quad (18)$$

1 where $\bar{\mathbf{d}}$ is the ensemble mean innovation and NOBS is the number of observations. For a well-
 2 tuned system, this “chi-squared” diagnostic should equal one (Ménard et al., 2000). Since the
 3 SPREAD is tuned to match a subset of the elements of the state vector rather than the entire state
 4 vector, we do not expect $\overline{\chi^2}$ to be exactly one, but it should be relatively close, at least in the
 5 time-average. For these experiments, $\overline{\chi^2}$ (not shown) starts out slightly high, but levels out to a
 6 time-mean (averaged from 2-10 days) of 0.99 for EnKF- uv and 0.97 for EnKF- $\psi\chi$.

7
 8 In Fig. 8, the analysis errors are projected onto the GW and RW modes. As expected from the
 9 imbalance calculations, the uninitialized EnKF- uv has much larger GW error due to larger
 10 imbalance in the increments. However, the EnKF- uv has slightly smaller RW errors. This is
 11 consistent with the initialized EnKF- uv having slightly larger WEP than the initialized EnKF- $\psi\chi$
 12 (Fig. 7a). This difference may be partly due to background error estimation biases caused by the
 13 $\psi\chi$ -localization, as discussed in Kepert (2009). These biases will either outweigh or
 14 underweigh the background at different scales, resulting in a suboptimal solution. We could try
 15 to correct for this effect by altering the observation error covariance as in Kepert (2009), but this
 16 does not account for the scale dependence of the bias. The situation in our case is also
 17 complicated by the adaptive inflation, which uses different state variables in EnKF- uv and
 18 EnKF- $\psi\chi$.

19
 20 Figure 9 (column 1) presents several global error diagnostics versus localization length (L) for
 21 Experiment 1. We define the “optimal” runs for each experiment as those that maximize WEP.
 22 These are indicated by squares (triangles) for uninitialized (initialized) results in Fig. 9a and are
 23 also listed in Table 1. In Fig. 9a and b the uninitialized WEP and zonal wind errors (meridional
 24 wind errors are very similar and are not shown) exhibit strong dependence on L , with maximum
 25 WEP occurring at $L = 1500$ km for EnKF- uv and $L = 2500$ km for EnKF- $\psi\chi$. The optimal EnKF-
 26 $\psi\chi$ run results in larger WEP and smaller wind error compared EnKF- uv , which would appear to
 27 favor the choice of $\psi\chi$ or uv . However, EnKF- $\psi\chi$ is much more sensitive to variations in L ,
 28 with WEP values actually becoming negative at small and large L .

1
2 Figure 9c shows a height error minimum at $L = 2000$ km for uninitialized EnKF- $\psi\chi$, while for
3 uninitialized EnKF- uv the height error increases monotonically with L . The increase of height
4 error with L is driven by the increase of imbalance with L , as seen in Fig. 9d. This increase in
5 imbalance with longer L when assimilating only ozone observations is a new finding, which is
6 opposite to the tendency of localization to create imbalance when assimilating dynamical
7 observations, as will be shown in Experiment 2 and discussed by Mitchell et al. (2002) and
8 Kepert et al. (2009, 2011). It is likely that ozone observations cause increased imbalance with L
9 due to spurious ensemble correlation between ozone and the dynamical variables at large
10 distances, which are projected onto the gravity modes. Up to $L = 4000$ km, the EnKF- uv has
11 larger imbalance than EnKF- $\psi\chi$, which is consistent with the single-observation simulations.
12 The ozone errors (Fig. 9e) show a broad minimum, with the EnKF- uv providing slightly better
13 values at all L .

14
15 After application of NMI, for both EnKF- uv and EnKF- $\psi\chi$ the wind and height errors are
16 smaller and WEP is larger at all values of L . The ozone error does not change, since the NMI is
17 applied only to the dynamical fields. The initialized results show WEP maximizing at $\sim 84\%$ for
18 EnKF- uv and $\sim 81\%$ for EnKF- $\psi\chi$ (see triangles on Fig. 9a). The length scales corresponding to
19 these values increase to 2000 km for EnKF- uv and 3500 km for EnKF- $\psi\chi$, suggesting the
20 correlations at larger lengths are more reliable. That EnKF- uv outperforms EnKF- $\psi\chi$ when NMI
21 is applied is consistent with Kepert (2009), who showed that EnKF- uv (with NMI) resulted in
22 smaller height and wind errors than the EnKF- $\psi\chi$ (with NMI) due to background error
23 estimation biases caused by the $\psi\chi$ -localization.

24
25 Up to this point, we have examined globally-averaged analysis errors. To determine regional
26 impact, we also examine how the errors vary with latitude for Experiment 1, shown in Fig. 10
27 (column 1). The initial wind errors (black lines in Fig. 10a and b) are largest in the NH tropics
28 and midlatitudes and near the North Pole (global maps of initial wind and height errors are
29 provided in Fig. 3 of Allen et al., 2014). After assimilating ozone, the uninitialized wind errors
30 are reduced at most latitudes. Small increases in uninitialized zonal wind error occur near 70°S

1 and 70°N. That the tropical bias has been removed is important, since the tropical winds are not
2 as well constrained in the stratosphere by radiance observations alone. The uninitialized height
3 errors (Fig. 10c) are more uniform after ozone assimilation, and show slight improvement in
4 some regions. However, uninitialized height errors have also increased over large portions of the
5 globe, particularly for EnKF- uv . This is due largely to the imbalance generated by the ozone
6 observations. Results with NMI (dotted lines on Fig. 10a-c) show reduced height (and wind)
7 errors at all latitudes compared to the original analyses, due to removal of spurious GW. Ozone
8 errors (Fig. 10d) are also reduced at all latitudes in this ozone assimilation experiment, with
9 slightly larger errors in the tropics.

10 4.2 Experiment 2: height only

11 We now examine the results of Experiment 2, when only height data are assimilated. For both
12 EnKF- uv and EnKF- $\psi\chi$, Fig. 9 (column 2) shows that WEP initially increases and wind errors
13 decrease with less localization (larger L), with optimal values occurring at $L = 5000$ km for
14 EnKF- uv and $L = 7000$ km for EnKF- $\psi\chi$, followed by a slight degradation at larger lengths. The
15 EnKF- $\psi\chi$ generally performs better than EnKF- uv . The minimum wind errors are ~ 1.3 m s⁻¹ for
16 EnKF- uv and 1.0 m s⁻¹ for EnKF- $\psi\chi$, which are reasonable values for a well-constrained
17 stratospheric analysis. For example, Hertzog et al. (2004) compared NH stratospheric analyses
18 with observations from long-duration balloon flights and calculated error SDs of the zonal wind
19 components of ~ 1.3 m s⁻¹ for ECMWF and ~ 1.9 m s⁻¹ for NCEP, when the observations were
20 low-pass filtered to remove the variance due to inertia-gravity waves.

21
22 The biggest difference between Experiments 1 and 2 is that assimilation of height observations
23 results in much less imbalance (note different vertical scales in Fig. 9d and 9i). The imbalance,
24 like the wind and height errors, generally decreases with less localization, which is opposite to
25 what occurred in Experiment 1. However, this is consistent with previous studies that have
26 examined balance in the EnKF in the context of assimilation of dynamical variables (e.g.,
27 Mitchell et al., 2002). This result provides a caution that while reducing the localization may
28 reduce imbalance for some observations, it may increase imbalance when assimilating ozone.
29 Applying NMI to the analyses results in almost no change to the WEP and wind errors, but does
30 improve the height errors, particularly for EnKF- uv .

1
2 The errors as a function of latitude for Experiment 2 are shown in Figure 10 (column 2). The
3 wind errors (Fig. 10e and f) are largest in the tropics and decrease towards the poles. This is
4 expected, since the height is more strongly correlated with wind in the extratropics due to
5 geostrophic balance. In the tropics this balance breaks down, and it is more difficult for the
6 EnKF to correct the winds with height observations alone. The analyzed height errors (Fig. 10g)
7 are markedly reduced from the initial errors, with slightly larger values in the extratropics.
8 Experiment 2 also improves the ozone, but only by a small amount (Fig. 10h). The small ozone
9 improvement is in the extratropics, likely due to more accurate winds that drive ozone advection.

10 4.3 Experiment 3: ozone and height

11 The final experiment examines the value of adding ozone assimilation to the analyses produced
12 by the height only assimilation. The results as a function of L are shown in Fig. 9 (column 3).
13 This experiment results in the smallest errors and highest WEP values, confirming that ozone
14 and height observations provide complimentary information to the DA system. Large WEP
15 values occur for a broad range of L , indicating that the results are not very sensitive to the choice
16 of localization length. The lowest uninitialized wind errors occur at $L = 3500$ km for both EnKF-
17 uv and EnKF- $\psi\chi$, and the maximum uninitialized WEP ($\sim 87\%$) is larger than when either ozone
18 or height are assimilated separately. The application of NMI slightly increases the optimal WEP
19 to $\sim 90\%$ for both systems.

20
21 The uninitialized height error and imbalance for Experiment 3 (Fig. 9m and n) show broad
22 minima, which reflects the combined tendencies of the height observations to increase imbalance
23 at small L and the ozone observations to increase imbalance at large L . The imbalance remains
24 relatively low in these experiments (< 20 m for $L < 5000$ km), with the EnKF- uv showing
25 somewhat higher values than EnKF- $\psi\chi$. The error in initialized height (dashed lines of Fig. 9m)
26 does show a significant decrease, suggesting that there is some GW noise in Experiment 3, but it
27 is much less than when ozone is assimilated alone. It appears that combining height observations
28 with ozone observations reduces the GW that would otherwise be generated by the ozone
29 observations alone.

30

1 The errors as a function of latitude for the optimal results from Experiment 3 are presented in
2 Fig. 10 (column 3). Wind errors are quite small ($< 0.5 \text{ m s}^{-1}$) across the globe, with the primary
3 benefit occurring in the tropics, where wind errors are much less than either Experiment 1 or 2.
4 The ozone in Experiment 3 is also better than Experiment 1. Having a better background ozone
5 field (due to better winds) allows more efficient use of the ozone observations. This likely
6 provides a positive feedback in the system that enhances the ozone impact. The addition of ozone
7 also tends to flatten height errors with latitude. Application of NMI does not impact the wind
8 errors very much, but does reduce the height errors as seen in Fig. 10k.

9
10 Additional experiments (not shown) were performed with a much smaller height error SD of 10
11 m. Decreasing the height error for height-only assimilation increased the maximum WEP to 84%
12 for EnKF- uv and 89% for EnKF- $\psi\chi$. The impact of adding ozone assimilation in these
13 experiments was also positive, increasing the maximum WEP to 92% for EnKF- uv and 91% for
14 EnKF- $\psi\chi$, with most of the wind improvements occurring in the tropics. These results suggest
15 that even in a very well-tuned system, high quality ozone observations can, in principle, improve
16 the winds.

17 **5. Conclusions**

18
19 The EnKF DA is able to employ cross-correlations between state variables in the ensemble
20 background states to couple tracer and dynamical variables. This study examined several aspects
21 of extraction of wind information from EnKF ozone assimilation using a shallow water model
22 (SWM) coupled with ozone advection. Three sets of experiments were performed that
23 assimilated ozone, geopotential height, or both. Modest improvements to the winds were
24 observed when either ozone or height were assimilated separately. Final WEP values of 46%
25 (58%) were obtained for ozone and 60% (69%) for height with the EnKF- uv (EnKF- $\psi\chi$) system.
26 When NMI was applied to the ozone experiment, WEP jumped to 84% (81%), showing that
27 gravity wave noise was generating significant error. The NMI applied to the height experiment
28 resulted in WEP increases of less than 1%, suggesting very small imbalance.

29

1 When assimilating both ozone and height, WEP rose to ~87% for both systems. Imbalance was
2 also much less than when ozone was assimilated alone. The addition of height observations
3 appears to reduce the gravity wave noise in the EnKF DA, thereby reducing the need for
4 initialization. This is important, since over-filtering could be a problem if NMI is applied to the
5 upper stratosphere/mesosphere (Sankey et al., 2007) and the tropics (Nezlin et al., 2009), where
6 unbalanced modes play an important role in the real atmosphere (see also Koshyk et al., 1999).
7 Applying NMI to the combined experiment resulted in a modest increase in WEP to ~90%. The
8 greatest impact of ozone assimilation on the winds was found to occur in the tropics, which are
9 less well constrained by height assimilation due to lack of geostrophy.

10
11 This study also compared results from EnKF systems that used different flow variables. While
12 the EnKF- uv system with ozone observations generated greater imbalance, this system was also
13 able to more accurately determine the wind structure of the rotational wave modes. This may be
14 due to biases in the specification of the background error covariance in the ENKF- $\psi\chi$, as
15 discussed by Kepert (2009). As a result, when NMI was applied, the EnKF- uv performed slightly
16 better than the EnKF- $\psi\chi$. For height assimilation, the EnKF- $\psi\chi$ performed better, due to less
17 imbalance, while the combined assimilation of ozone and height produced similar results in the
18 two systems.

19
20 In each experiment the localization length was tuned to maximize the wind extraction. Previous
21 studies have shown that tighter localization increases imbalance, which may be detrimental. We
22 showed that while this was the case for height observations, for ozone observations the imbalance
23 actually increased with localization length. The cause is uncertain, but may be due to spurious
24 long-range correlations between ozone and the dynamical fields, which project onto the gravity
25 modes of the SWM.

26
27 While under the ideal conditions used in this study WEP values of up to ~90% were achieved
28 (wind component errors $\sim 0.3 \text{ m s}^{-1}$), there are many challenges to demonstrating that the ozone-
29 wind coupling in operational DA system can be beneficial. There are observation system
30 challenges such as frequency, latency, precision, and bias. There are also modeling challenges
31 such as accurate ozone transport, chemistry, and radiation. The results here were obtained with a

1 single-layer model, relatively low resolution (T42), and a rather simple wave-forcing scenario.
2 Given these caveats, this study demonstrated ozone-wind interaction in the EnKF and the
3 potential for ozone assimilation to benefit the wind analysis, particularly in the tropics.

4
5 Whether 4D-Var or EnKF is better for ozone-wind extraction is still an open question. In our
6 previous work we showed that wind extraction is feasible when assimilating globally-gridded
7 hourly tracer data (ozone, nitrous oxide, or water vapor) within 4D-Var. Follow-up experiments
8 (not presented here) indicate that ozone-wind extraction is also possible in 4D-Var assimilation
9 of the ozone and height data used here. In future work, we plan to directly compare 4D-Var,
10 EnKF, and hybrid methods for tracer-wind extraction.

11 **Acknowledgments**

12
13 We would like to thank Alan Geer, one anonymous reviewer, and the editor for helpful
14 comments on the manuscript. This work was funded by the U. S. Office of Naval Research.

15 **References**

16 Allen, D. R., Hoppel, K. W., Nedoluha, G. E., Kuhl, D. D., Baker, N. L., Xu, L., and Rosmond,
17 T. E.: Limitations of wind extraction from 4D-Var assimilation of ozone, *Atmos. Chem. Phys.*,
18 13, 3501-3515, doi:10.5194/acp-13-3501-2013, 2013.

19 Allen, D. R., Hoppel, K. W., and Kuhl, D. D.: Wind extraction potential from 4D-Var
20 assimilation of stratospheric O₃, N₂O, and H₂O using a global shallow water model, *Atmos.*
21 *Chem. Phys.*, 14, 3347-3360, doi:10.5194/acp-14-3347-2014, 2014.

22 Anderson, J. L.: An adaptive covariance inflation error correction algorithm for ensemble filters,
23 *Tellus*, 59A, 210-224, doi:10.1111/j.1600-0870.2006.00216.x, 2007.

24 Andersson, E., E. Hólm, P. Bauer, A. Beljaars, G. A. Kelly, A. P. McNally, A. J. Simmons, J.-N.
25 Thépaut, and Tompkins, A. M.: Analysis and forecast impact of the main humidity observing
26 systems, *Q. J. Roy. Meteor. Soc.*, 133, 1473-1485, doi:10.1002/qj.112, 2007.

27 Andrews, D. G., Holton, J. R., and Leovy, C. B.: *Middle Atmosphere Dynamics*, Academic
28 Press, Inc., Orlando, Florida, USA, 1987.

1 Baker, W. E., Atlas, R., Cardinali, C., Clement, A., Emmitt, G. D., Gentry, B. M., Hardesty, R.
2 M., Källén, E., Kavaya, M. J., Langland, R., Ma, Z., Masutani, M., McCarty, W., Pierce, R. B.,
3 Pu, Z., Riishojgaard, L. P., Ryan, J., Tucker, S., Weissmann, M., and Yoe, J. G.: Lidar-measured
4 wind profiles: the missing link in the global observing system, *Bull. Amer. Meteor. Soc.*, 95(4),
5 543-564, doi:10.1175/bams-d-12-00164.1, 2014.

6 Bonavita, M., Isaksen, L., and Hólm, E., ‘On the use of EDA background error variances in the
7 ECMWF 4D-Var,’ ECMWF Tech Memo 664. Available at
8 <http://old.ecmwf.int/publications/library/do/references/show?id=90381> (last access: 21 April
9 2015), 2012.

10 Buehner, M., Houtekamer, P. L., Charette, C., Mitchell, H. L., and He, B.: Intercomparison of
11 variational data assimilation and the ensemble Kalman filter for global deterministic NWP. Part
12 II: One-month experiments with real observations, *Mon. Wea. Rev.*, 138, 1567-1586,
13 doi:10.1175/2009MWR3158.1, 2010.

14 Clayton, A. M., Lorenc, A. C., and Barker, D. M.: Operational implementation of a hybrid
15 ensemble/4D-Var global data assimilation system at the Met Office, *Q. J. R. Meteorol. Soc.*, 139,
16 1445–1461. doi:10.1002/qj.2054, 2013.

17 Courtier P., and Talagrand, O.: Variational assimilation of meteorological observations with the
18 direct and adjoint shallow-water equations, *Tellus*, 42A, 531-549, doi: 10.1034/j.1600-
19 0870.1990.t01-4-00004.x, 1990.

20 Daley, R.: Estimating the wind-field from chemical-constituent observations - experiments with
21 a one-dimensional extended Kalman filter, *Mon. Wea. Rev.*, 123, 181-198, doi: 10.1175/1520-
22 0493(1995)123<0181:ETWFFC>2.0.CO;2, 1995.

23 Daley, R.: Recovery of the one and two dimensional windfields from chemical constituent
24 observations using the constituent transport equation and an extended Kalman filter, *Meteorol.*
25 *Atmos. Phys.*, 60, 119-136, 1996.

26 Dragani, R., and McNally, A. P.: Operational assimilation of ozone-sensitive infrared radiances
27 at ECMWF, *Q. J. Roy. Meteor. Soc.*, 139, 2068-2080, doi:10.1002/qj.2106, 2013.

28 Evensen, G.: The ensemble Kalman filter: theoretical formulation and practical implementation,
29 *Ocean Dynamics*, 53, 343-367, doi:10.1007/s10236-003-0036-9, 2003.

1 Fillion, L., Mitchell, H. L., Ritchie, H., and Staniforth, A.: The impact of a digital filter
2 finalization technique in a global data assimilation system, *Tellus*, 47A, 304-323, doi:
3 10.1034/j.1600-0870.1995.t01-2-00002.x, 1995.

4 Gaspari, G., and Cohn, S. E.: Construction of correlation functions in two and three dimensions,
5 *Q. J. Roy. Meteor. Soc.*, 125, 723-757, doi:10.1002/qj.49712555417, 1999.

6 Han, W., and McNally, A. P.: The 4D-Var assimilation of ozone-sensitive infrared radiances
7 measured by IASI, *Q. J. Roy. Meteor. Soc.*, 136, 2025-2037, doi:10.1002/qj.708, 2010.

8 Hertzog, A., Basdevant, C., Vial, F., and Mechoso, C. R.: The accuracy of stratospheric analyses
9 in the northern hemisphere inferred from long-duration balloon flights, *Q. J. Roy. Meteor. Soc.*,
10 130, 607-626, doi:10.1256/qj.03.76, 2004.

11 Hogan, T. F., Rosmond, T. E., and Gelaro, R., 'The NOGAPS forecast model: a technical
12 description,' NRL Publication AD-A247 216, 218 pp. Naval Research Laboratory: Monterey,
13 California, USA, Available at <http://www.dtic.mil/docs/citations/ADA247216> (last access: 5
14 February 2015), 1992.

15 Houtekamer, P. L., and Mitchell, H. L.: Data assimilation using an ensemble Kalman filter
16 technique, *Mon. Wea. Rev.*, 126, 796-811, doi: 10.1175/1520-
17 0493(1998)126<0796:Dauaek>2.0.Co;2, 1998.

18 Houtekamer, P. L., and Mitchell, H. L.: A sequential ensemble Kalman filter for atmospheric
19 data assimilation, *Mon. Wea. Rev.*, 129, 123-137, doi: 10.1175/1520-
20 0493(2001)129<0123:Asekff>2.0.Co;2, 2001.

21 Jung, B.-J, Kim, S., and Jo, Y.: Representer-based variational data assimilation in a spectral
22 element shallow water model on the cubed-sphere grid, *Tellus A*, 66, 24493,
23 doi:10.3402/tellusa.v66.24493, 2014.

24 Kepert, J. D.: Covariance localisation and balance in an ensemble Kalman filter, *Q. J. Roy.*
25 *Meteor. Soc.*, 135, 1157-1176, doi:10.1002/qj.443, 2009.

26 Kepert, J. D.: Balance-aware covariance localisation for atmospheric and oceanic ensemble
27 Kalman filters, *Comput. Geosci.*, 15, 239-250, doi:10.1007/s10596-010-9188-0, 2011.

1 Kleist, D. T., Parrish, D. F., Derber, J. C., Treadon, R., Errico, R. M., and Yang, R.: Improving
2 incremental balance in the GSI 3DVAR analysis system, *Mon. Wea. Rev.*, 137, 1046-1060,
3 doi:10.1175/2008MWR2623.1, 2009.

4 Kleist, D. T., and Ide, K.: An OSSE-based evaluation of hybrid variational-ensemble data
5 assimilation for the NCEP GFS. Part II: 4DEnVar and hybrid variants, *Mon. Wea. Rev.*, 143,
6 452-470, doi:10.1175/MWR-D-13-00350.1, 2015.

7 Koshyk, J. N., and Hamilton, K.: The horizontal kinetic energy spectrum and spectral budget
8 simulated by a high-resolution troposphere-stratosphere-mesosphere GCM, *J. Atmos. Sci.*, 58,
9 329-348, doi:10.1175/1520-0469(2001)058<0329:Thkesa>2.0.Co;2, 2001.

10 Kuhl, D. D., Rosmond, T. E., Bishop, C. H., McLay, J., and Baker, N. L.: Comparison of Hybrid
11 Ensemble/4DVar and 4DVar within the NAVDAS-AR data assimilation framework, *Mon. Wea.*
12 *Rev.*, 141, 2740-2758, doi:10.1175/MWR-D-12-00182.1, 2013.

13 Limpasuvan, V., Thompson, D. W. J, and Hartmann, D. L.: The life cycle of the Northern
14 Hemisphere sudden stratospheric warmings, *J. Climate*, 17, 2584-2596, doi: 10.1175/1520-
15 0442(2004)017<2584:Tlcotn>2.0.Co;2, 2004.

16 Livesey N.J., Read, W.G., Froidevaux, L., Lambert, A., Manney, G.L., Pumphrey, H.C., Santee,
17 M.L., Schwartz, M.J., Wang, S., Cofield, R.E., Cuddy, D.T., Fuller, R.A., Jarnot, R.F., Jiang,
18 J.H., Knosp, B.W., Stek, P.C., Wagner, P.A., and Wu, D.L.: ‘Earth Observing System (EOS)
19 Aura Microwave Limb Sounder (MLS) Version 3.3 Level 2 data quality and description
20 document,’ JPL D-33509, 162 pp., Jet Propulsion Laboratory, Pasadena, California, USA,
21 Available at http://mls.jpl.nasa.gov/data/v3-3_data_quality_document.pdf (last access: 5
22 February 2015), 2001.

23 Lorenc, A. C.: The potential of the ensemble Kalman filter for NWP – a comparison with 4D-
24 Var, *Q. J. Roy. Meteor. Soc.*, 129, 3183-3203, doi:10.1256/qj.02.132, 2003.

25 Machenhauer, B.: On the dynamics of gravity oscillations in a shallow water model, with
26 applications to normal mode initialization, *Contrib. Atmos. Phys.*, 50, 253-271, 1977.

27 Ménard, R., Cohn, S. E., Chang, L.-P., and Lyster, P. M.: Assimilation of chemical tracer
28 observations using a Kalman filter. Part I: Formulation, *Mon. Wea. Rev.*, 128, 2654-2671, doi:
29 10.1175/1520-0493(2000)128<2654:Aoscto>2.0.Co;2, 2000.

1 Milewski, T., and Bourqui, M. S.: Assimilation of stratospheric temperature and ozone with an
2 ensemble Kalman filter in a chemistry-climate model, *Mon. Wea. Rev.*, 139, 3389-3404,
3 doi:10.1175/2011mwr3540.1, 2011.

4 Mitchell, H. L., and Houtekamer, P. L.: Ensemble size, balance, and model-error representation
5 in an ensemble Kalman filter, *Mon. Wea. Rev.*, 130, 2791-2808, doi: 10.1175/1520-
6 0493(2002)130<2791:Esbame>2.0.Co;2, 2002.

7 National Research Council: Earth Science and Applications from Space: National Imperatives
8 for the Next Decade and Beyond, National Academy Press, Washington, DC, 428 pp., available
9 at http://www.nap.edu/catalog.php?record_id=11820 (last access: 5 February 2015), 2007.

10 Neef, L. J., Polavarapu, S. M., and Shepherd, T. G.: Four-dimensional data assimilation and
11 balanced dynamics, *J. Atmos. Sci.*, 63, 1840-1858, doi:10.1175/jas3714.1, 2006.

12 Neef, L. J., Polavarapu, S. M., and Shepherd, T. G.: A low-order model investigation of the
13 analysis of gravity waves in the ensemble Kalman filter, *J. Atmos. Sci.*, 66, 1717-1734,
14 doi:10.1175/2008jas2585.1, 2009.

15 Nezlin, Y., Rochon, Y. J., and Polavarapu, S.: Impact of tropospheric and stratospheric data
16 assimilation on the mesosphere, *Tellus*, 61A, 154-159, doi:10.1111/j.1600-0870.2008.00368.x,
17 2009.

18 Norton, W.A.: Breaking Rossby waves in a model stratosphere diagnosed by a vortex-following
19 coordinate system and a technique for advecting material contours, *J. Atmos. Sci.*, 51, 644-673,
20 doi:10.1175/1520-0469(1994)051<0654:BRWIAM>2.0.CO;2, 1994.

21 Peubey, C., and McNally, A. P.: Characterization of the impact of geostationary clear-sky
22 radiances on wind analyses in a 4D-Var context, *Q. J. Roy. Meteor. Soc.*, 135, 1863-1876, doi:
23 doi:10.1002/qj.500, 2009.

24 Peuch, A., Thepaut, J. N., and Pailleux, J.: Dynamical impact of total-ozone observations in a
25 four-dimensional variational assimilation, *Q. J. Roy. Meteor. Soc.*, 126, 1641-1659, doi:
26 10.1002/qj.49712656605, 2000.

27 Polavarapu, S., Tanguay, M., and Fillion, L.: Four-dimensional variational data assimilation with
28 digital filter initialization, *Mon. Wea. Rev.*, 128, 2491-2510, doi: 10.1175/1520-
29 0493(2000)128<2491:FDVDAW>2.0.CO;2, 2000.

1 Riishøjgaard, L. P.: On four-dimensional variational assimilation of ozone data in weather-
2 prediction models, *Q. J. Roy. Meteor. Soc.*, 122, 1545-1571, doi:10.1002/qj.49712253505, 1996.

3 Ritchie, H.: Application of the semi-Lagrangian method to a spectral model of the shallow water
4 equations, *Mon. Wea. Rev.*, 116, 1587-1598, doi: 10.1175/1520-
5 0493(1988)116<1587:AOTSLM>2.0.CO;2, 1988.

6 Sankey, D., Ren, S., Polavarapu, S., Rochon, Y. J., Nezlin, Y., and Beagley, S.: Impact of data
7 assimilation filtering methods on the mesosphere, *J. Geophys. Res.*, 112, D24104,
8 doi:10.1029/2007JD008885, 2007.

9 Semane, N., Peuch, V. H., Pradier, S., Desroziers, G., El Amraoui, L., Brousseau, P., Massart, S.,
10 Chapnik, B., and Peuch, A.: On the extraction of wind information from the assimilation of
11 ozone profiles in Meteo-France 4-D-Var operational NWP suite, *Atmos. Chem. Phys.*, 9, 4855-
12 4867, doi:10.5194/acp-9-4855-2009, 2009.

13 Stoffelen, A., Pailleux, J., Kallen, E., Vaughan, J. M., Isaksen, L., Flamant, P., Wergen, W.,
14 Andersson, E., Schyberg, H., Culoma, A., Meynard, R., Endemann, M., and Ingmann, P.: The
15 atmospheric dynamics mission for global wind field measurement. *Bull. Amer. Meteorol. Soc.*,
16 86, 73-87, doi:10.1175/bams-86-1-73, 2005.

17 Waters, J. W., Read, W. G., Froidevaux, L., Jarnot, R. F., Cofield, R. E., Flower, D. A., Lau, G.
18 K., Pickett, H. M., Santee, M. L., Wu, D. L., Boyles, M. A., Burke, J. R., Lay, R. R., Loo, M. S.,
19 Livesey, N. J., Lungu, T. A., Manney, G. L., Nakamura, L. L., Perun, V. S., Ridenoure, B. P.,
20 Shippony, Z., Siegel, P. H., and Thurstans, R. P.: The UARS and EOS Microwave Limb Sounder
21 (MLS) experiments, *J. Atmos. Sci.*, 56, 194-218, doi: 10.1175/1520-
22 0469(1999)056<0194:TUAEML>2.0.CO;2, 1999.

23 Williamson, D. L., and Temperton, C.: Normal mode initialization for a multilevel grid-point
24 model. Part II: nonlinear aspects, *Mon. Wea. Rev.*, 109, 744-757, doi: 10.1175/1520-
25 0493(1981)109<0744:Nmifam>2.0.Co;2, 1981.

26 World Meteorological Organization: Statement of guidance regarding how well satellite
27 capabilities meet WMO user requirements in several application areas, *WMO Satellite Rep*,
28 SAT-22, 29 pp, Available at

- 1 http://library.wmo.int/opac/index.php?lvl=notice_display&id=11446#.U-5jq2Pb70c (last access:
- 2 5 February 2015), 2000.
- 3

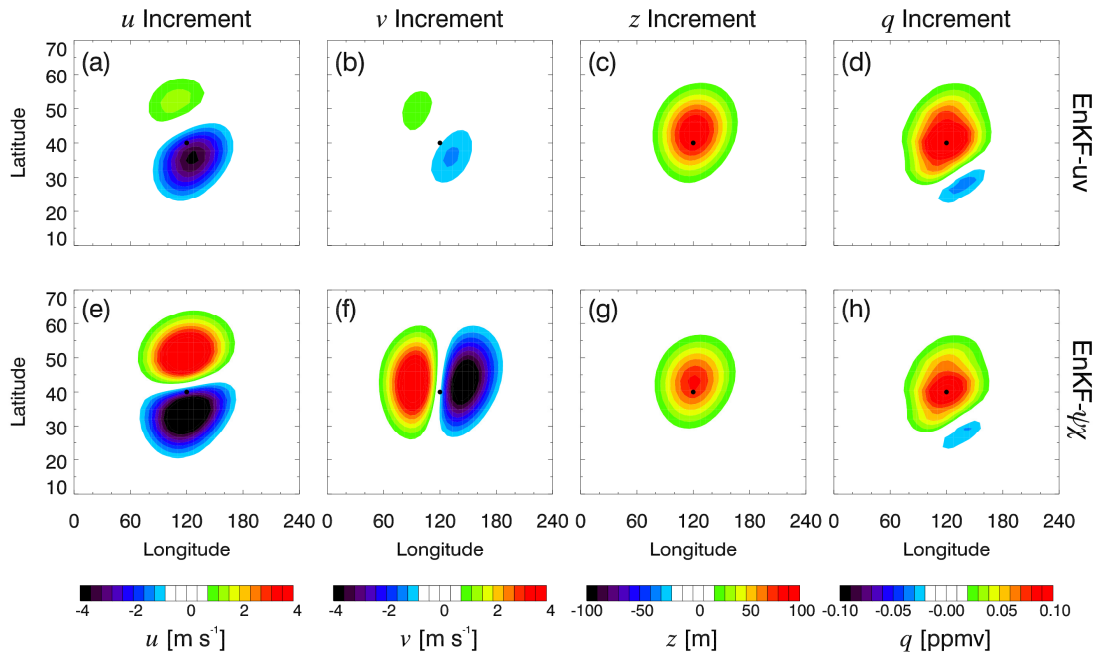
1

Experiment	L (km)	WEP (%)	u error (m s^{-1})	v error (m s^{-1})	z error (m)	q error (ppmv)
1. Ozone						
uv	1500	45.5	1.58	1.59	60.9	0.054
$\psi\chi$	2500	57.8	1.25	1.25	42.7	0.070
uv (NMI)	2000	83.7	0.55	0.46	14.4	0.047
$\psi\chi$ (NMI)	3500	80.6	0.62	0.58	12.8	0.058
2. Height						
uv	5000	59.5	1.27	1.38	11.6	0.179
$\psi\chi$	7000	68.8	0.96	1.05	7.8	0.150
uv (NMI)	5000	60.4	1.25	1.35	6.8	0.179
$\psi\chi$ (NMI)	7000	69.1	0.95	1.04	6.1	0.150
3. Both						
uv	3500	86.7	0.40	0.41	11.0	0.039
$\psi\chi$	3500	87.5	0.37	0.39	8.5	0.040
uv (NMI)	3500	90.1	0.32	0.31	2.6	0.039
$\psi\chi$ (NMI)	4500	89.5	0.33	0.32	2.8	0.041

2

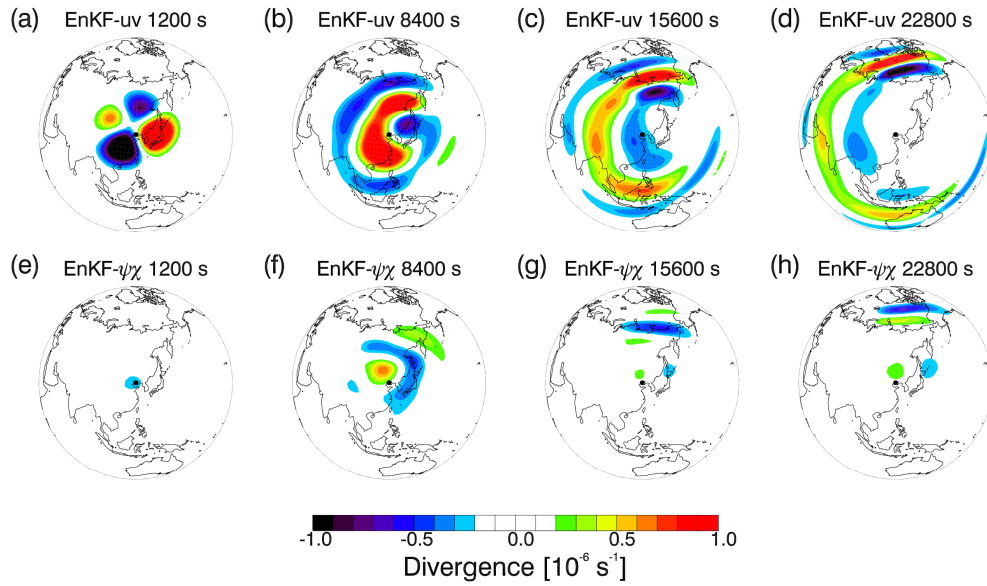
3 **Table 1.** Results for the optimal runs (i.e., maximum wind extraction potential (WEP)), for each
4 experiment. The localization length (L) is provided along with WEP and global mean root mean
5 square error (RMSE) for u , v , z , and q . NMI refers to normal mode initialization applied to the
6 analysis fields.

7



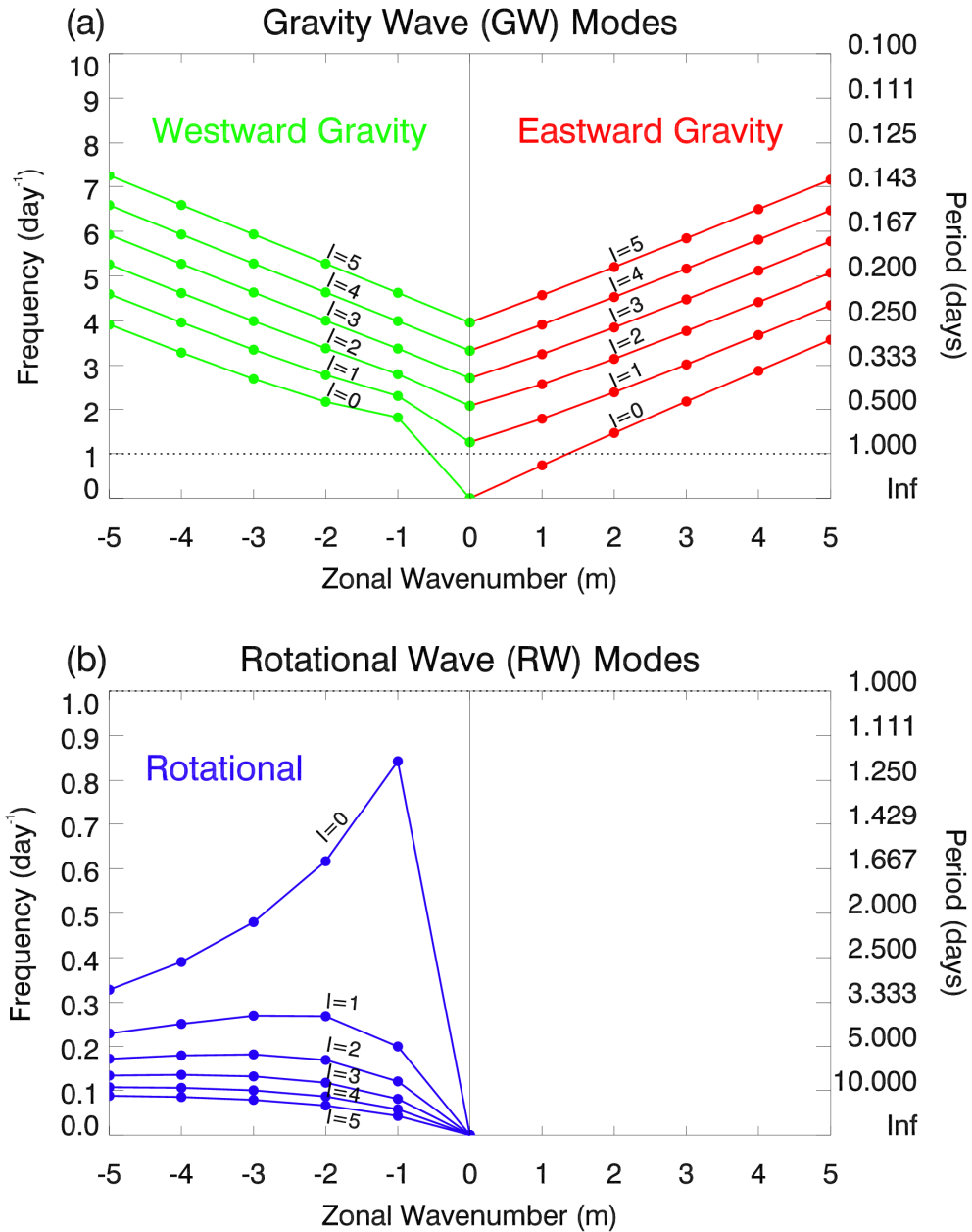
1
 2 **Fig. 1.** Analysis increments due to assimilation of a single ozone observation (time = 1200 s) at
 3 120°E, 40°N (indicated by black dot) using EnKF- uv (top row) and EnKF- $\psi\chi$ (bottom row) with
 4 localization length $L = 2000$ km. Variables are given by column: zonal wind (u [m s^{-1}], column
 5 1), meridional wind (v [m s^{-1}], column 2), height (z [m], column 3), and ozone (q [ppmv],
 6 column 4). Red (blue) contours indicate high (low) values for each variable.

7

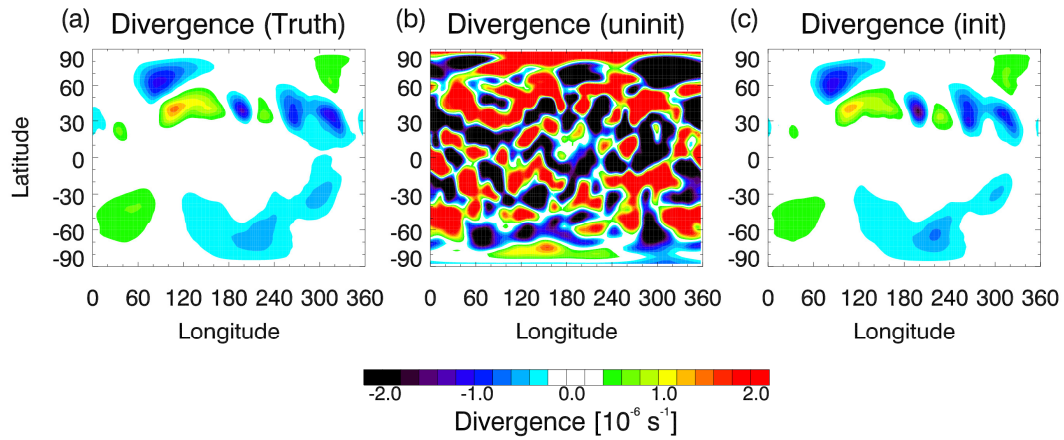


1
 2 **Fig. 2.** Divergence anomalies [10^{-6} s^{-1}] due to single-observation increments (see Fig. 1) at time
 3 = 1200 s, 8400 s, 15600 s, and 22800 s for EnKF- uv (top row) and EnKF- $\psi\chi$ (bottom row). Red
 4 (blue) contours indicate high (low) values of divergence.

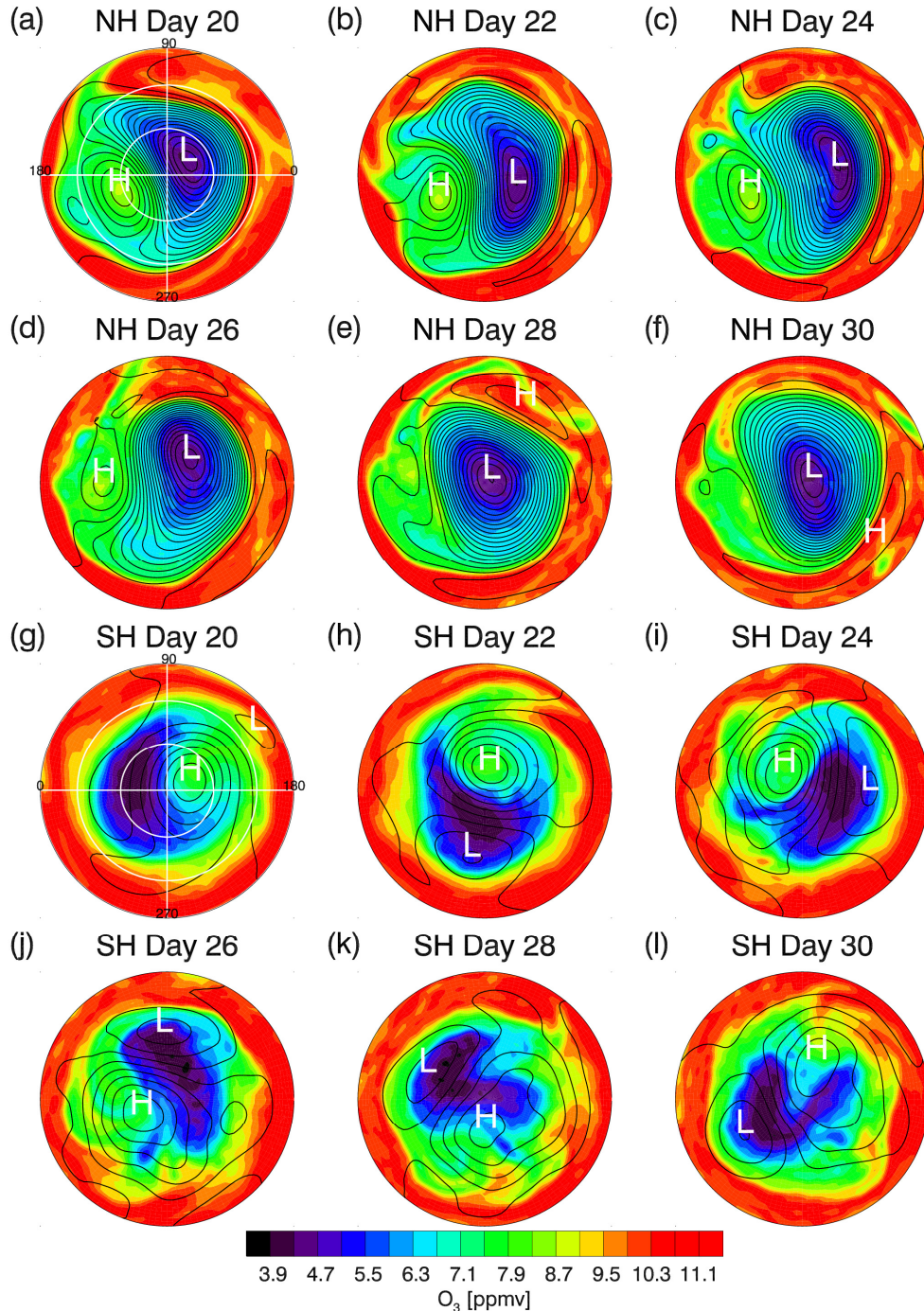
5



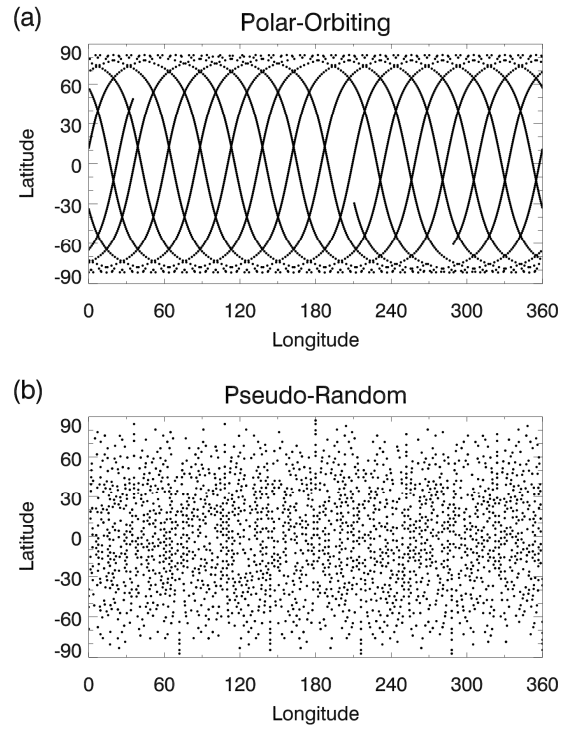
1
2 **Fig. 3.** The normal mode frequencies [day^{-1}] for the spectral SWM at triangular truncation T42 as
3 a function of zonal wavenumber (m) for the first six values of the meridional wavenumber $l = n -$
4 $l = |m|$, where n is the total wavenumber. Positive (negative) values of m indicate eastward
5 (westward) motion. Modes are separated into (a) eastward and westward gravity wave (GW)
6 modes, and (b) rotational wave (RW) modes. There are no rotational modes for positive m (see
7 section 2.3). The cutoff frequency (1.0 day^{-1}) for the NMI is indicated by the dotted line. Note
8 that the frequency scales are different for the two plots for easier viewing.



1
 2 **Fig. 4.** Divergence [10^{-6} s^{-1}] maps for the (a) truth run (TR), (b) uninitialized analysis, and (c)
 3 initialized analysis from day 2 of Experiment 1 with EnKF- uv and localization length $L = 2000$
 4 km. For each plot, red (blue) contours indicate high (low) values.
 5

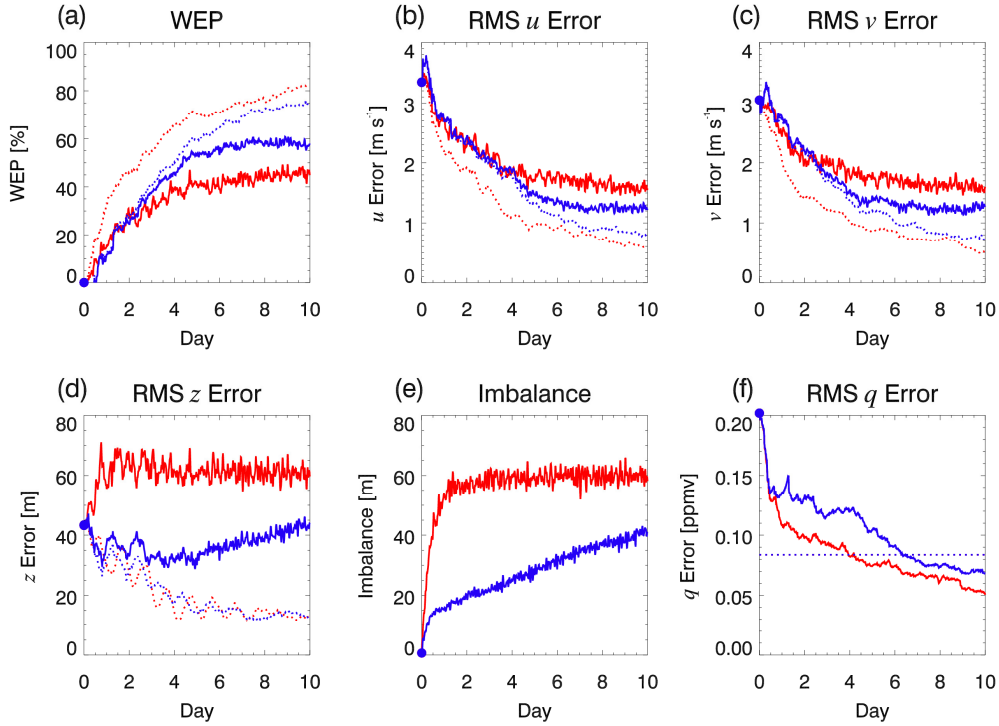


1
 2 **Fig. 5.** Maps of ozone [ppmv] (colors) overlaid with height (black lines) at 200 m intervals for
 3 days 20, 22, 24, 26, 28, and 30 of the truth run (TR). (a) – (f) are NH and (g) – (l) are SH. The
 4 plots for day 20 include longitude (latitude) grid lines at 90° (30°) intervals, with 0°, 90°, 180°,
 5 and 270° longitude marked. The hemispheric maximum and minimum heights are indicated by
 6 “H” and “L”, respectively. For each plot, red (blue) contours indicate high (low) ozone values.



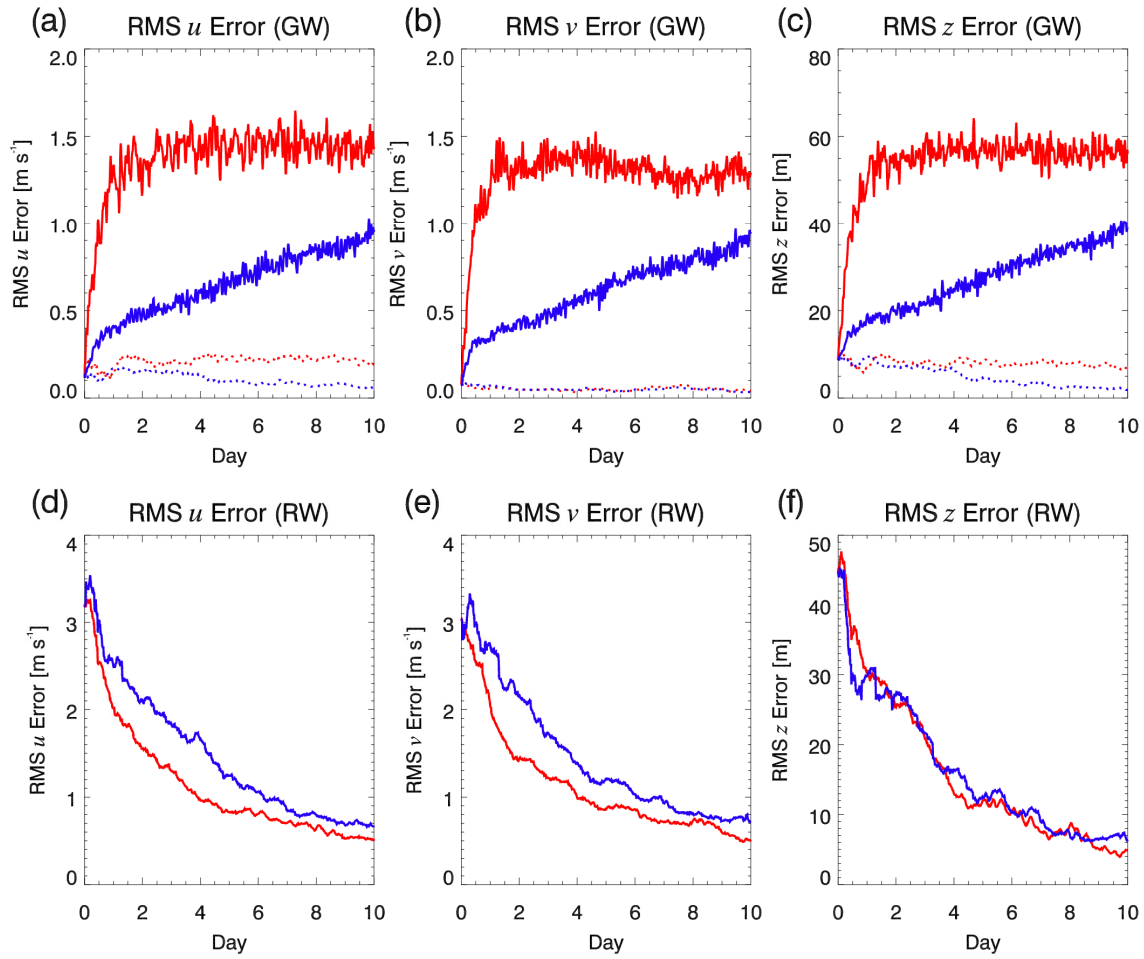
1
2
3
4

Fig. 6. Sampling patterns for 24 h of (a) polar-orbiting ozone data and (b) pseudo-random height data.



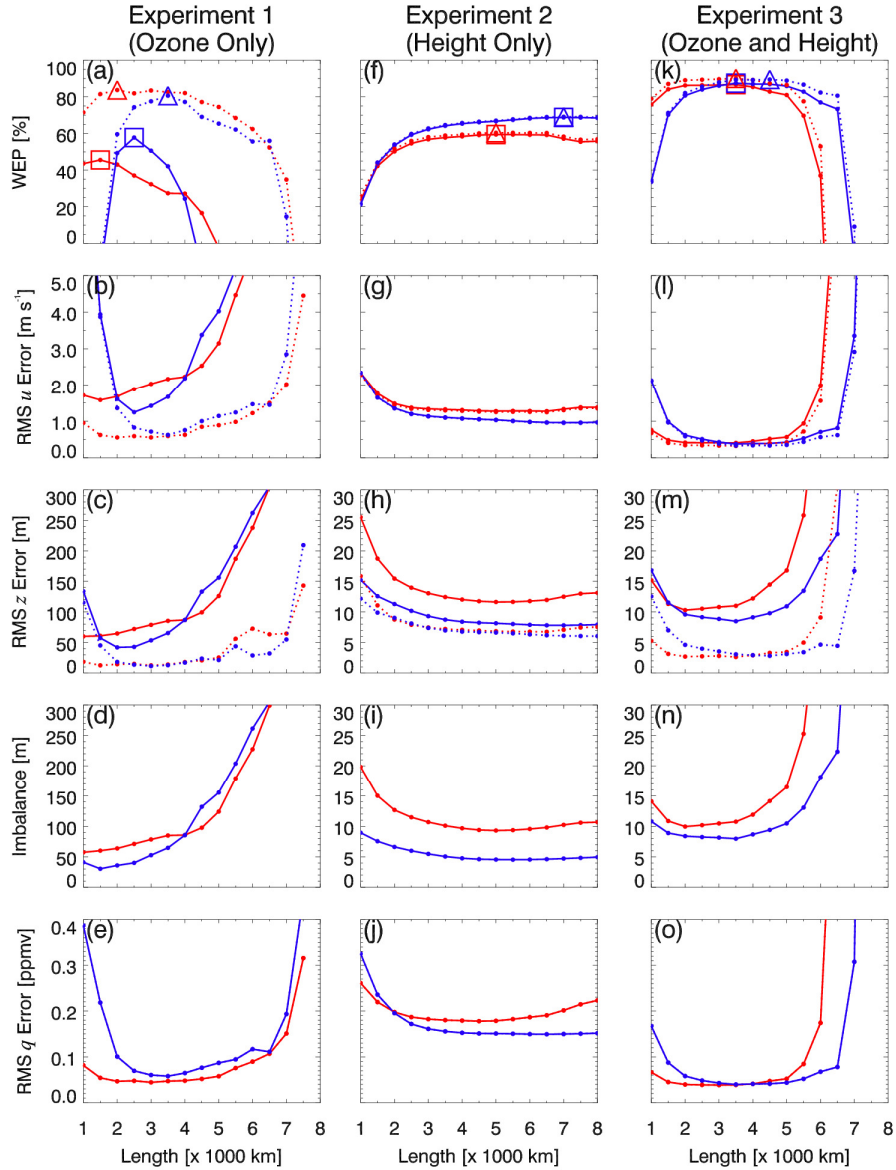
1
2 **Fig. 7.** Diagnostics from optimal runs of Experiment 1: Ozone only ($L = 1500$ km for EnKF- uv
3 and $L = 2500$ km for EnKF- $\psi\chi$). (a) WEP [%], (b), (c), and (d) RMS errors for u [$m s^{-1}$], v [$m s^{-1}$],
4 and z [m], respectively, (e) Imbalance [m], and (f) RMS error for q [ppmv]. EnKF- uv is red
5 and EnKF- $\psi\chi$ is blue. Solid (dotted) lines indicate uninitialized (initialized) results (there are no
6 dotted lines in (f) because the ozone error does not change, since the NMI is applied only to the
7 dynamical fields). In (f) the ozone observation error standard deviation is indicated by the
8 horizontal dotted line. Blue circles at day 0 indicate the initial values.

9



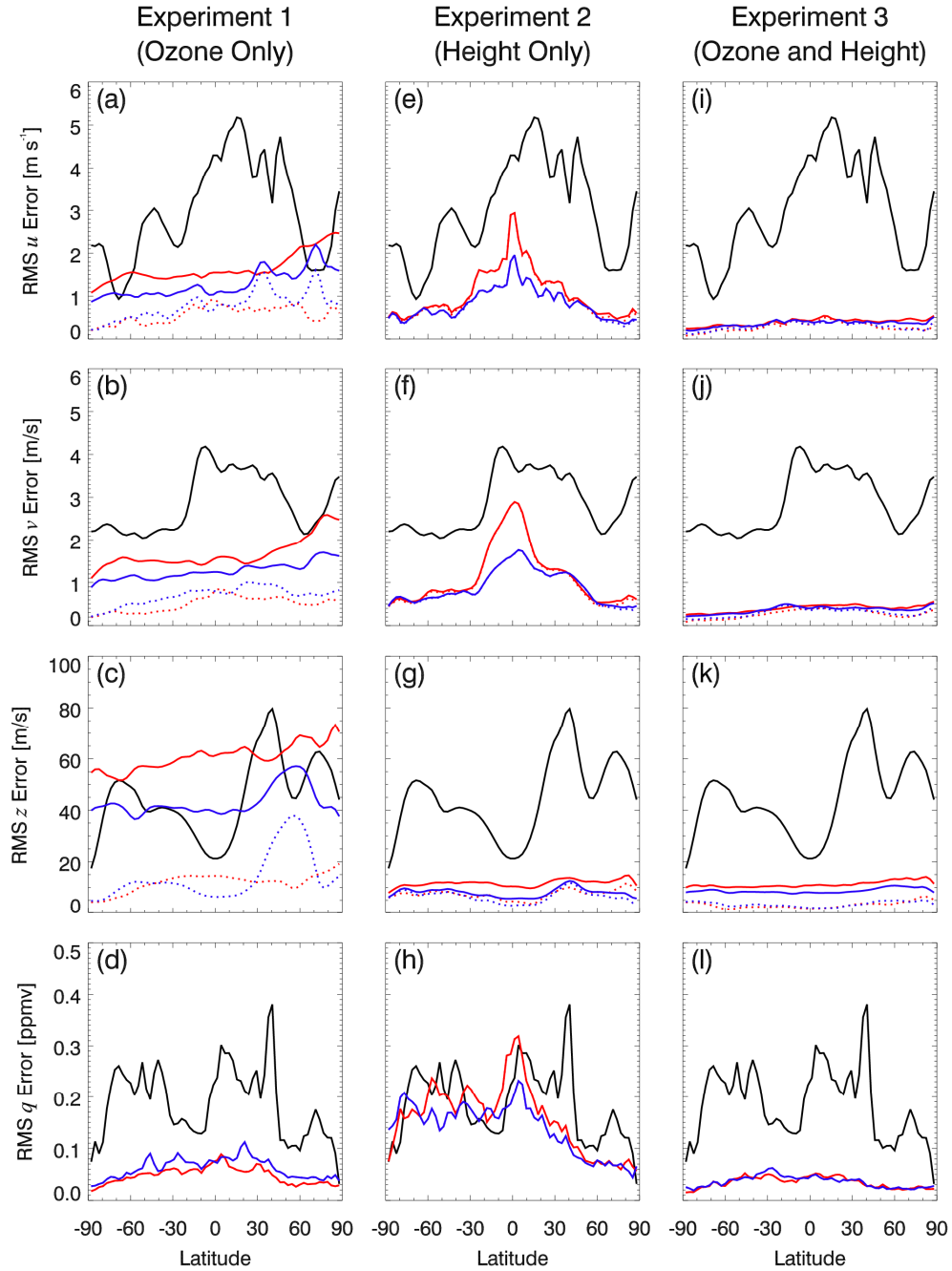
1
2
3
4
5
6

Fig. 8. RMS errors for u [m s⁻¹], v [m s⁻¹], and z [m] (columns 1, 2, and 3, respectively) for gravity wave (GW) modes (row 1) and rotational wave (RW) modes (row 2) for the optimal runs of Experiment 1: Ozone only with EnKF- uv (red) and EnKF- $\psi\chi$ (blue). Solid (dotted) lines indicate uninitialized (initialized) results.



1
2 **Fig. 9.** WEP [%] (row 1), RMS errors for u [m s^{-1}], v [m s^{-1}], z [m], and q [ppmv] (rows 2, 3, and
3 5, respectively), and Imbalance [m] (row 4) as a function of localization length (L) for
4 Experiments 1, 2, and 3 (columns 1, 2, and 3, respectively). Red is for EnKF- uv and blue is for
5 EnKF- $\psi\chi$. Solid (dotted) lines indicate uninitialized (initialized) results (there are no dotted
6 lines in row 5, because the ozone error does not change, since the NMI is applied only to the
7 dynamical fields). The optimal runs (i.e., maximum WEP) values are highlighted with squares
8 (triangles) for uninitialized (initialized) results in row 1.

9
10



1
2 **Fig. 10.** RMS errors as a function of latitude for u [m s^{-1}], v [m s^{-1}], z [m], and q [ppmv] (rows 1,
3 2, 3, and 4, respectively) for the optimal runs (as shown in Table 1 and in the highlighted squares
4 of Fig. 9) of Experiments 1, 2, and 3 (columns 1, 2, and 3, respectively). Black lines show initial
5 errors and red (blue) lines show EnKF- uv (EnKF- $\psi\chi$) errors. Solid (dotted) lines indicate
6 uninitialized (initialized) results (there are no dotted lines in row 4 because the ozone error does
7 not change, since the NMI is applied only to the dynamical fields).